Fast and Accurate Poisson Denoising with Optimized Nonlinear Diffusion

Wensen Feng and Yunjin Chen

arXiv:1510.02930v1 [cs.CV] 10 Oct 2015

***Abstract*—The degradation of the acquired signal by Poisson noise is a common problem for various imaging applications, such as medical imaging, night vision and microscopy. Up to now, many state-of-the-art Poisson denoising techniques mainly concentrate on achieving utmost performance, with little consideration for the computation efficiency. Therefore, in this study we aim to propose an efficient Poisson denoising model with both high computational efficiency and recovery quality. To this end, we exploit the newly-developed trainable nonlinear reaction diffusion model which has proven an extremely fast image restoration approach with performance surpassing recent state-of-the-arts. We retrain the model parameters, including the linear filters and influence functions by taking into account the Poisson noise statistics, and end up with an optimized nonlinear diffusion model specialized for Poisson denoising. The trained model provides strongly competitive results against state-of-the-art approaches, meanwhile bearing the properties of simple structure and high efficiency. Furthermore, our proposed model comes along with an additional advantage, that the diffusion process is well-suited for parallel computation on GPUs. For images of size 512×512, our GPU implementation takes less than 0.1 seconds to produce state-of-the-art Poisson denoising performance.**

***Index Terms*—Poisson denoising, optimized nonlinear reaction diffusion model, convolutional neural networks, trained activation functions**

I. Introduction

IMAGE degradation by Poisson noise is unavoidable in real applications such as astronomy imaging, biomedical imaging, and microscopy, among many others [3], [27], [2]. Therefore, the Poisson noise removal is of crucial importance, especially when data is to be submitted to further processing e.g. image segmentation and recognition. Due to the physical mechanism, the strength of the Poisson noise depends on the image intensity and is therefore not additive, alluding to the fact that Poisson denoising is generally quite different from the usual case of the additive noise.

Up to now, a host of Poisson denoising algorithms has been proposed in the literature, see [7], [11], [9], [33] and the references therein for a survey. Roughly speaking, major contributions consist of two classes: (1) with variance stabilizing transformation (VST) and (2) without VST.

The approaches in the first class preprocess the input data by applying a nonlinear VST such as Anscombe [1], [8] or Fisz [10] which help remove the signal-dependency property of the Poisson noise. The noise characteristic of the transformed data can be approximately regarded as signal-independent additive Gaussian noise. Then, many well-studied Gaussian denoising algorithms can be employed to estimate a clean image for the transformed image. Finally, the estimate of the underlying noise-free image is obtained by applying an inverse VST [32], [19], [22], [23] to the denoised transformed data. Using the well-known BM3D algorithm [6] for Gaussian noise removal, the resulting Poisson denoising algorithm leads to state-of-the-art performance. However, the VST is accurate only when the measured pixels have relative high intensity. That is to say, the recover error using the VST will dramatically increase for cases of low-counts [29], especially for extremely low-count cases e.g., images with peak $= 0.1$.

In order to deal with the aforementioned deficiency of the VST operation, several authors [31] [29] [12] have investigated denoising strategies without VST, which rely directly on the statistics of the Poisson noise. In [29], J. Salmon $et\ al.$ proposed a novel denoising algorithm in combination of elements of dictionary learning and sparse patch-based representations, which relies directly on Poisson noise properties. It employs both an adaptation of Principal Component Analysis (PCA) for Poisson noise [25] and sparse Poisson intensity estimation methods [14] in a non-local framework. This direct approach achieves state-of-the-art results for images suffering from a high noise level. There are two versions involved in this method: the non-local PCA (NLPCA) and the non-local sparse PCA (NL-SPCA). Particularly, the NL-SPCA results in a better image restoration performance by integrating an ℓ_1 regularization term to the minimized objective.

Similarly, to overcome the deficiency of VST, the data-fidelity term originated from Poisson noise statistics is adopted in [9], [17], [12]. Especially, the work in [12] relies on the Poisson statistical model directly and uses a dictionary learning strategy with a sparse coding algorithm that employs a boot-strapping based a stopping criterion. The reported denoising performance of the method proposed in [12] is competitive with leading methods.

A. Our Contribution

While having a closer look at state-of-the-art Poisson denoising approaches, we find that such approaches mainly concentrate on achieving utmost image restoration quality, with little consideration on the computational efficiency. A notable exception is the BM3D based algorithm incorporation with VST operation [23], which meanwhile offers high

W.S. Feng is with School of Automation and Electrical Engineering, University of Science and Technology Beijing, Beijing, 100083, China. e-mail: (wensenfeng1986@gmail.com)

Y.J. Chen is with National Laboratory for Parallel and Distribution Processing National University of Defense Technology Deyalu 47, 410073 Changsha, Hunan Province, China e-mail: (chenyunjin_nudt@hotmail.com)

Corresponding author: Yunjin Chen.

efficiency, thanks to the highly engineered and well refined BM3D algorithm.

The goal of our work is to develop a simple but effective approach with both high computational efficiency and competitive denoising quality with state-of-the-art approaches. To this end, we employ the newly-developed trainable nonlinear reaction diffusion model [4] which has several remarkable benefits. First, this model is merely a standard nonlinear diffusion model with trained filters and influence functions, and therefore achieves very high levels of recovery quality surpassing recent state-of-the-arts. Second, it needs only a small number of explicit steps, and hence is extremely fast and highly computationally efficient. Furthermore, it is well suited for parallel computation on GPUs. The employed model [4] can also be interpreted as a recurrent convolutional neural networks (CNN) [13] with trainable activation functions. The standard CNN models typically fix the activation function and just train the filters. Differently, the employed model simultaneously optimizes the filters and the nonlinear activation functions, and therefore has a great potential to improve the performance of the standard CNN models.

In this paper, we start with an energy functional derived from the Poisson noise distribution, and derive a trainable nonlinear diffusion process specialized for the task of Poisson denoising. The model parameters in the diffusion process need to be trained by taking into account the Poisson noise statistics, including the linear filters and influence functions. Eventually, we reach a nonlinear reaction diffusion based approach for Poisson denoising, which leads to state-of-the-art performance, meanwhile gains high computationally efficiency. Moreover, the straightforward direct gradient descent employed for Gaussian denoisng task [4] is not applicable in our study. To solve this problem, we resort to the proximal gradient descent method [26].

B. Organization

The remainder of the paper is organized as follows. Section II presents a general review of the statistics property of Poisson noise, the trainable nonlinear reaction diffusion process and the proximal gradient method, which is required to derive the diffusion process for Poisson denoising. In the subsequent section III, we propose the optimized nonlinear diffusion process for poisson noise reduction. Subsequently, Section IV describes comprehensive experiment results for the proposed model. The concluding remarks are drawn in the final Section V.

II. Preliminaries

To make the paper self-contained, in this section we provide a brief review of Poisson noise, the trainable nonlinear diffusion process proposed in [4] and the basic update rule of the proximal gradient algorithm [26].

A. Poisson Noise

Suppose that $f \in \mathbb{Z}_+^N$ (represented as a column-stacked vector) denotes a Poisson noisy image and $u \in \mathbb{R}^N$ is the original true image of interest. Our task is to recover u from f. Each observed pixel value f_i in f given u_i in u is assumed to be a Poisson distributed independent random variable with mean and variance u_i, i.e.,

$$P\left(f_i|u_i\right) = \begin{cases} \frac{{u_i}^{f_i}}{f_i!}\exp\left(-u_i\right), & u_i > 0 \\ \delta_0\left(f_i\right), & u_i = 0, \end{cases} \tag{II.1}$$

where u_i and f_i are the i-th component in u and f respectively, and δ_0 is the Kronecker delta function. As is known, Poisson noise is signal dependent, due to the fact that the strength of the noise is proportional to the signal intensity u_i. Therefore, the noise level in the image u is generally defined as the peak value (the maximal value) in u. This is reasonable since the effect of Poisson noise increases (i.e., the signal-to-noise ratio (SNR) decreases) as the intensity value u_i decreases.

Minimizing the negative log-likelihood $E = -\log P(f|u)$ of (II.1) leads to the following data-fidelity term in the variational framework

$$\langle u - f\log u, 1\rangle, \tag{II.2}$$

where $\langle , \rangle$ denotes the standard inner product. This data-fidelity term (II.2) is also known as the so-called Csiszár I-divergence model [5], and has been widely investigated in previous Poisson denoising algorithms, e.g., [29], [14], [20].

B. Trainable Nonlinear Reaction Diffusion

A simple but effective framework for image restoration based on the concept of nonlinear diffusion was recently proposed in our previous work [4], which extends conventional nonlinear reaction diffusion models by several parameterized linear filters as well as several parameterized influence functions. The proposed framework in [4] is formulated as a time-dynamic nonlinear reaction-diffusion model, having the following general form

$$\begin{cases} u_0 = I_0 \\ u_{t+1} = u_t - \underbrace{\sum_{i=1}^{N_k} \bar{k}_i^t * \phi_i^t(k_i^t * u_t)}_{\text{diffusion term}} - \underbrace{\psi(u_t, f)}_{\text{reaction term}}, t = 0 \cdots T-1 \,, \end{cases} \tag{II.3}$$

where $*$ is the convolution operation, T denotes the diffusion stages, k_i are time varying convolution kernels ($\bar{k}_i$ are obtained by rotating the kernel k_i 180 degrees), ϕ_i^t are time varying influence functions (not restricted to be of a certain kind), $\psi(u_t, f)$ is the reaction term, and N_k is the number of filters. The reaction term can be typically chosen as the derivative of a date term $\mathcal{D}(u, f)$, i.e., $\psi(u) = \nabla_u \mathcal{D}(u, f)$. I_0 is the initial status of the diffusion process, and can be set as f. Note that the diffusion behavior of each step in the model (II.3) can be different.

The framework (II.3) has wide applicability for various image restoration problems by incorporating specific data terms. For example, it is easy to handle classical image restoration problems, such as Gaussian denoising, image deblurring, image super resolution and image inpainting, by setting $\mathcal{D}(u, f) = \frac{\lambda}{2}\|Au - f\|_2^2$, $\psi(u) = \lambda A^\top(Au - f)$, where f is the input degraded image, A is the associated linear

operator[1], and λ is related to the strength of the reaction term. For the problem of Poisson denoising exploited in this paper, the data term should be chosen as follows according to (II.2).

$$\mathcal{D}(u, f) = \lambda \langle u - f \log u, 1 \rangle . \tag{II.4}$$

At each time step t, the employed model (II.3) can be interpreted as performing one gradient descent step at u^t with respect to a certain energy functional given by

$$E(u, f) = \sum_{i=1}^{N_k} \sum_{p=1}^{N} \rho_i^t((k_i^t * u)_p) + \mathcal{D}(u, f) , \tag{II.5}$$

where the functions $\{\rho_i^t\}_{t=0}^{t=T-1}$ are the so-called penalty functions. Note that $\rho'(z) = \phi(z)$ and $k_i * u$ denotes 2D convolution of the image u with the filter kernel k_i. Since the parameters $\{k_i^t, \rho_i^t\}$ vary across the stages, (II.5) is a dynamic energy functional, which changes at each iteration.

The employed diffusion model is closely related to the convolutional networks (CNs) employed for image restoration problems [16]. It can be treated as a convolutional network because each iteration (stage) of the diffusion process involves the convolution operation with a set of linear filters. The architecture of the employed diffusion model is shown in Figure 1, and can be categorized into recurrent networks [13] with trainable activation functions. Besides, the special CNN architecture with trained activation functions has also been proposed in [15]. The work in [15] aims at ImageNet Classification and achieves surpassing Human-Level performance. However, the trainable activation function in [15] is parameterized by only one free variable, while in the employed diffusion model there are several free parameterized variables to learn.

The employed diffusion model is trained in a supervised manner, namely we firstly prepare the input/output pairs for certain image processing task, and then exploit a loss minimization scheme to learn the model parameters Θ^t for each stage t of the diffusion process. The training dataset consists of S training samples $\{f^s, u_{gt}^s\}_{s=1}^S$, where f^s is a degraded input and u_{gt}^s is the corresponding ground truth clean image. The model parameters Θ^t of each stage include the parameters of (1) the reaction force weight λ, (2) linear filters and (3) influence functions, i.e., $\Theta^t = \{\lambda^t, \phi_i^t, k_i^t\}$. The training task is formulated as the following optimization problem

$$\begin{cases} \min\limits_{\Theta} \mathcal{L}(\Theta) = \sum\limits_{s=1}^{S} \ell\left(u_T^s, u_{gt}^s\right) = \sum\limits_{s=1}^{S} \frac{1}{2}\|u_T^s - u_{gt}^s\|_2^2 \\ \text{s.t.} \begin{cases} u_0^s = f^s \\ u_{t+1}^s = u_t^s - \sum\limits_{i=1}^{N_k} \bar{k}_i^t * \phi_i^t(k_i^t * u_t^s) - \psi(u_t^s, f^s), t = 0 \cdots T-1 , \end{cases} \end{cases} \tag{II.6}$$

where $\Theta = \{\Theta^t\}_{t=0}^{t=T-1}$. The training problem can be solved via gradient based algorithms, e.g., commonly used L-BFGS algorithm [21]. The gradients of the loss function with respect to Θ_t are computed using the standard back-propagation technique widely used in the neural networks learning [18]. There are two training strategies to learn the diffusion processes: 1) the greedy training strategy to learn the diffusion process stage-by-stage; and 2) the joint training strategy to joint train all the stages simultaneously. Generally speaking, the joint training strategy performs better [4], and the greedy training strategy is often employed to provide a good initialization for the joint training. For simplicity, we just consider the joint training scheme to train a diffusion process by simultaneously tuning the parameters in all stages. The associated gradient $\frac{\partial \ell(u_T, u_{gt})}{\partial \Theta_t}$ is presented as follows,

$$\frac{\partial \ell(u_T, u_{gt})}{\partial \Theta_t} = \frac{\partial u_t}{\partial \Theta_t} \cdot \frac{\partial u_{t+1}}{\partial u_t} \cdots \frac{\partial \ell(u_T, u_{gt})}{\partial u_T} . \tag{II.7}$$

One can refer to [4] and its supplementary materials for the detailed calculation process of $\frac{\partial u_t}{\partial \Theta_t}$ and $\frac{\partial u_{t+1}}{\partial u_t}$.

C. The Proximal Gradient Method

In order to derive the diffusion process for Poisson denoising, we start with the energy functional (II.5) by incorporating the data term (II.4). However, for this problem, the straightforward direct gradient descent $1 - \frac{f}{u}$ is not applicable in practice, because (1) it has an evident problem of numerical instability at the points with u very close to zero; (2) this update rule can not guarantee that the output image after one diffusion step is positive. Negative values of u will violate the constraint of the data term (II.4).

As a consequence, we resort to the proximal gradient descent method [26], which can avoid the formula $1 - \frac{f}{u}$, and thus solve the above two problems. The proximal gradient method is applicable to solve an optimization problem which is composed of a smooth function F and a convex (possibly non-smooth) function G:

$$\arg\min_u F(u) + G(u). \tag{II.8}$$

It is based on a forward-backward splitting scheme. The basic update rule to solve (II.8) is given as

$$u^{n+1} = \left(\mathbf{I} + \tau \partial G\right)^{-1} \left(u^n - \tau \nabla F\left(u^n\right)\right), \tag{II.9}$$

where τ denotes the step size parameter, and $u^n - \tau \nabla F\left(u^n\right)$ is the forward gradient descent step. The term $\left(\mathbf{I} + \tau \partial G\right)^{-1}$ denotes the standard proximal mapping [26], and is also the backward step. The proximal mapping $\left(\mathbf{I} + \tau \partial G\right)^{-1}(\tilde{u})$ with respect to G is given as the following minimization problem

$$\left(\mathbf{I} + \tau \partial G\right)^{-1}(\tilde{u}) = \arg\min_u \frac{\|u - \tilde{u}\|_2^2}{2} + \tau G(u) . \tag{II.10}$$

III. Optimized Nonlinear Diffusion Process for Poisson Noise Reduction

A. Proposed Diffusion Process for Poisson Denoising

In this section, we propose the optimized nonlinear reaction diffusion process for the task of Poisson denoising. First of all, it should be noted that the diffusion process can be interpreted as one gradient decent step of the energy functional (II.5). Therefore, we start from the following variational model by

[1]In the case of Gaussian denoising, A is the identity matrix; for image super resolution, A is related to the down sampling operation and for image deconvolution, A corresponds to the linear blur kernel.

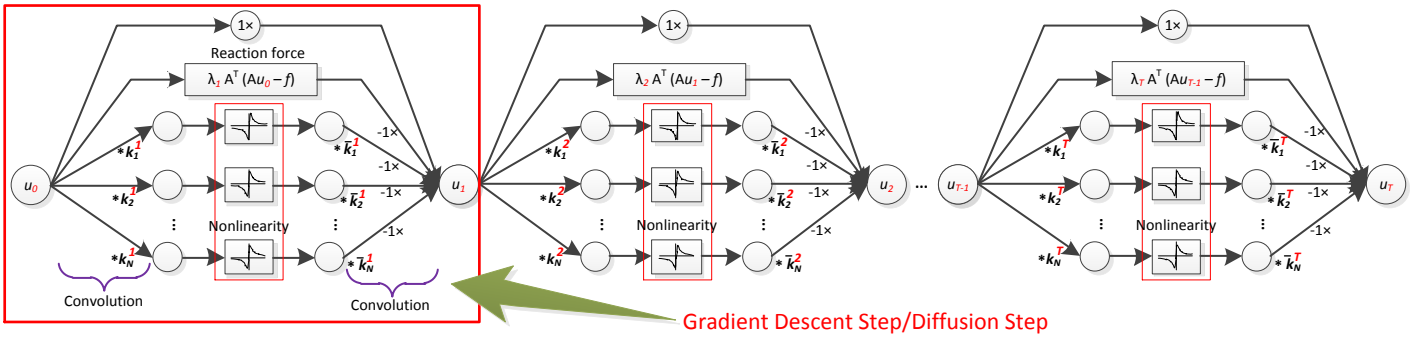

Fig. 1. The architecture of the employed diffusion model with a reaction term, e.g., $\psi(u_{t-1}, f) = A^\top(Au_{t-1} - f)$. It is represented as a feed-forward network.

combing the data-fidelity term (II.4),

$$\arg\min_{u>0} E(x) = \sum_{i=1}^{N_k} \sum_{p=1}^{N} \rho_i((k_i * u)_p) + \lambda\langle u - f\log u, 1\rangle\,. \tag{III.1}$$

As mentioned earlier, the straightforward direct gradient descent is not applicable for this problem. Therefore, we resort to the proximal gradient descent method to derive the corresponding diffusion process. Casting the problem (III.1) in the form of (II.8), we have $F(u) = \sum_{i=1}^{N_k} \sum_{p=1}^{N} \rho_i((k_i * u)_p)$ and $G(u) = \lambda\langle u - f\log u, 1\rangle$. It is easy to check that

$$\nabla F(u) = \sum_{i=1}^{N_k} K_i^\top \phi_i(K_i u),$$

where $K_i \in \mathbb{R}^{N\times N}$ is a highly sparse matrix, implemented as 2D convolution of the image u with the filter kernel k_i, i.e., $K_i u \Leftrightarrow k_i * u$, $\phi(K_i u) = (\phi(K_i u)_1, \cdots, \phi(K_i u)_N)^\top \in \mathbb{R}^N$, and $\rho'(z) = \phi(z)$. Note that in the case of symmetric boundary condition exploited in our work, $K_i^\top$ can be interpreted as the convolution kernel $\bar{k}_i$ only in the central region. As stated in [4], in order to simplify the diffusion model, it is better to revise the above formulation as explicit convolutions. Therefore, the gradient of F is revised as

$$\nabla F(u) \doteq \sum_{i=1}^{N_k} \bar{k}_i * \phi_i(k_i * u)\,.$$

Recall that $\bar{k}_i$ is a rotated version of 180 degrees of kernel k_i.

The proximal mapping with respect to G is given as the following minimization problem

$$(\mathbf{I} + \tau\partial G)^{-1}(\tilde{u}) = \arg\min_u \frac{\|u - \tilde{u}\|_2^2}{2} + \tau\lambda\langle u - f\log u, 1\rangle\,. \tag{III.2}$$

The solution of (III.2) is given by the following point-wise operation

$$\hat{u} = (\mathbf{I} + \tau\partial G)^{-1}(\tilde{u}) = \frac{\tilde{u} - \tau\lambda + \sqrt{(\tilde{u} - \tau\lambda)^2 + 4\tau\lambda f}}{2}\,. \tag{III.3}$$

Note that $\hat{u}$ is always positive if $f > 0$, i.e, this update rule can guarantee $\hat{u} > 0$ in diffusion steps.

As a consequence, the diffusion process for Poisson denoising using the proximal gradient method can be formulated as

$$u_{t+1} = \frac{\tilde{u}_{t+1} - \lambda^{t+1} + \sqrt{(\tilde{u}_{t+1} - \lambda^{t+1})^2 + 4\lambda^{t+1} f}}{2}, \tag{III.4}$$

where $\tilde{u}_{t+1} = u_t - \sum_{i=1}^{N_k} \bar{k}_i^{t+1} * \phi_i^{t+1}(k_i^{t+1} * u_t)$, and we set the step size $\tau = 1$.

B. Computing The Gradients for Training

In this subsection, we present the joint training strategy for poisson denoising.

First of all, the diffusion equation for Poisson denoising is as presented in (III.4), from which we can compute the gradients of the loss function w.r.t the training parameters $\Theta_t = \{\lambda^t, \phi_i^t, k_i^t\}$. According to (II.7), we should compute three parts of $\frac{\partial \ell(u_T, u_{gt})}{\partial \Theta_t}$, i.e., $\frac{\partial u_{t+1}}{\partial u_t}$, $\frac{\partial u_t}{\partial \Theta_t}$ and $\frac{\partial \ell(u_T, u_{gt})}{\partial u_T}$.

First of all, the gradients $\frac{\partial \ell(u_T, u_{gt})}{\partial u_T}$ is easy to calculate according to the training loss function. For example, in the case of quadratic training cost function, $\frac{\partial \ell(u_T, u_{gt})}{\partial u_T}$ is given as

$$\frac{\partial \ell(u_T, u_{gt})}{\partial u_T} = u_T - u_{gt}\,.$$

According to the chain rule, $\frac{\partial u_{t+1}}{\partial u_t}$ is computed as follows,

$$\frac{\partial u_{t+1}}{\partial u_t} = \frac{\partial \tilde{u}_{t+1}}{\partial u_t} \cdot \frac{\partial u_{t+1}}{\partial \tilde{u}_{t+1}}. \tag{III.5}$$

Starting from the update rule (III.4), it is easy to check that $\frac{\partial \tilde{u}_{t+1}}{\partial u_t}$ is given as

$$\frac{\partial \tilde{u}_{t+1}}{\partial u_t} = \mathbf{I} - \sum_{i=1}^{N_k} K_i^{t+1\top} \cdot \Lambda_i \cdot \left(\bar{K}_i^{t+1}\right)^\top. \tag{III.6}$$

where Λ_i is a diagonal matrix $\Lambda_i = \mathrm{diag}(\phi_i^{t\prime}(x_1), \cdots, \phi_i^{t\prime}(x_N))$ ($\phi_i^{t\prime}$ is the first order derivative of function ϕ_i^t), with $x = k_i^{t+1} * u_t$. Here, $\{x_i\}_{i=1}^{i=N}$ denote the element of x which is represented as a column-stacked vector. Note that in practice, we do not need to explicitly construct the matrices K_i and $\bar{K}_i$. As shown in [4], $K_i^\top$ and $\bar{K}_i^\top$ can be computed by the convolution operation with the kernel k_i and $\bar{k}_i$, respectively with careful boundary handling.

Then the part $\frac{\partial u_{t+1}}{\partial \tilde{u}_{t+1}}$ can be computed according to (III.4) and is formulated as

$$\frac{\partial u_{t+1}}{\partial \tilde{u}_{t+1}} = \mathrm{diag}(y_1, \cdots, y_N), \tag{III.7}$$

where $\{y_i\}_{i=1}^{i=N}$ denote the elements of

$$y = \frac{1}{2}\left[1 + \frac{\tilde{u}_{t+1} - \lambda^{t+1}}{\sqrt{(\tilde{u}_{t+1} - \lambda^{t+1})^2 + 4\lambda^{t+1} f}}\right].$$

Now, the $\frac{\partial u_{t+1}}{\partial u_t}$ is obtained by combing (III.6) and (III.7).

Concerning the gradients $\frac{\partial u_t}{\partial \Theta_t}$, as Θ_t involves $\{\lambda^t, \phi_i^t, k_i^t\}$, we can derive them respectively. It is worthy noting that the gradients of u_t w.r.t $\{\phi_i^t, k_i^t\}$ are only associated with $\tilde{u}_t = u_{t-1} - \sum_{i=1}^{N_k} \bar{k}_i^t * \phi_i^t(k_i^t * u_{t-1})$. Therefore, the gradient of u_t w.r.t ϕ_i^t and k_i^t is computed via

$$\frac{\partial u_t}{\partial \phi_i^t} = \frac{\partial \tilde{u}_t}{\partial \phi_i^t} \cdot \frac{\partial u_t}{\partial \tilde{u}_t},$$

and

$$\frac{\partial u_t}{\partial k_i^t} = \frac{\partial \tilde{u}_t}{\partial k_i^t} \cdot \frac{\partial u_t}{\partial \tilde{u}_t},$$

where the derivations of $\frac{\partial \tilde{u}_t}{\partial \phi_i^t}$ and $\frac{\partial \tilde{u}_t}{\partial k_i^t}$ have been provided in [4]. The gradients of $\frac{\partial u_t}{\partial \tilde{u}_t}$ are calculated similar to (III.7). The gradient of u_t w.r.t λ^t is computed as

$$\frac{\partial u_t}{\partial \lambda^t} = (z_1, \cdots, z_N), \tag{III.8}$$

where $\{z_i\}_{i=1}^{i=N}$ denote the elements of

$$z = \frac{1}{2}\left[-1 + \frac{(\lambda^t - \tilde{u}_t) + 2f}{\sqrt{(\tilde{u}_t - \lambda^t)^2 + 4\lambda^t f}}\right].$$

Note that $\frac{\partial u_t}{\partial \lambda^t}$ is written as a column vector.

In practice, in order to ensure the value of λ^t positive during the training phase, we set $\lambda = e^{\beta}$. As a consequence, in the programming we employ the gradient $\frac{\partial u_t}{\partial \beta^t}$ instead of $\frac{\partial u_t}{\partial \lambda^t}$. The gradient $\frac{\partial u_t}{\partial \beta^t}$ can be explicitly formulated as

$$\frac{\partial u_t}{\partial \beta^t} = \frac{\lambda^t}{2}\left[-1 + \frac{(\lambda^t - \tilde{u}_t) + 2f}{\sqrt{(\tilde{u}_t - \lambda^t)^2 + 4\lambda^t f}}\right]. \tag{III.9}$$

IV. Experiments

In this section, we considered the fully Trained Reaction Diffusion models for Poisson Denoising (TRDPD). The corresponding nonlinear diffusion process of stage T with filters of size $m \times m$ is expressed as $\mathrm{TRDPD}_{m\times m}^{T}$ whose number of filters is $m^2 - 1$ in each stage, if not specified.

To generate the training data for our denoising experiments, we cropped a 180×180 pixel region from each image of the Berkeley segmentation dataset [24], resulting in a total of 400 training samples of size 180 × 180. Of course, we also employ different amounts of training samples (e.g., 50-600 in Fig. 2) to observe the denoising performance comparison.

After training the models, we evaluate them on 68 test images originally introduced by [28], which have since become a reference set for image denoising. To provide a comprehensive comparison, the test peak values are distributed between 1 to 40.

Moreover, the proposed algorithm is compared with two representative state-of-the-art methods: the NLSPCA [29] and BM3D-based method with the exact unbiased inverse Anscombe [23], both with and without binning technique. The corresponding codes are downloaded from the author's homepage, and we use them as is. For the binning technique, we closely follow [29] and use a 3×3 ones kernel to increase the peak value to be 9 times higher, and a bilinear interpolation for the upscaling of the low-resolution recovered image. Two commonly used quality measures are taken to evaluate the Poisson denoising performance, i.e., PSNR and the structural similarity index (SSIM) [30]. Note that the PSNR values in the following three subsections are evaluated by averaging denoised results of 68 test images. For simplicity the test peak value is set as 40 in the following three contrastive analysises, without loss of generality.

A. Influence of Number of Training Samples

In this subsection, we evaluate the test performance of trained models using different amounts of training samples for $\mathrm{TRDPD}_{5\times5}^{5}$.

The results are summarized in Fig. 2, from which one can see that 350-400 images are typically enough to provide reliable performance. It is also worthy noting that too small training set will result in over-fitting which leads to inferior PSNR value.

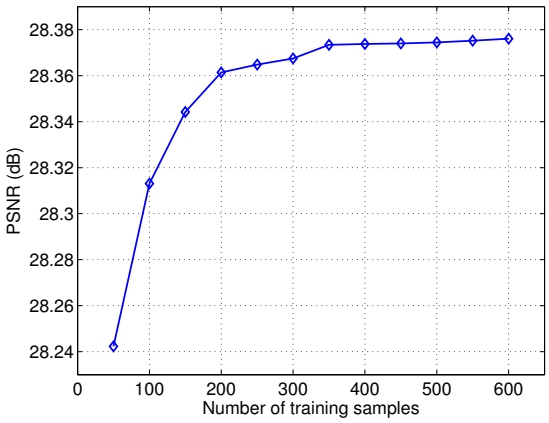

Fig. 2. Influence of the number of training examples.

B. Influence of filter size

We also investigate the influence of the filter size on the denoising performance in Fig. 3. The diffusion stages are set as 5, and 400 images are used for training.

One can see that increasing the filter size from 3×3 to 5×5 brings a significant improvement. However, a much smaller PSNR gain (≤ 0.01) is achieved if we increase the filter size from 7×7 to 9×9. By evaluating the training time and the performance improvement, we prefer the $\mathrm{TRDPD}_{7\times7}^{T}$ model as it provides the best trade-off between performance and training time.

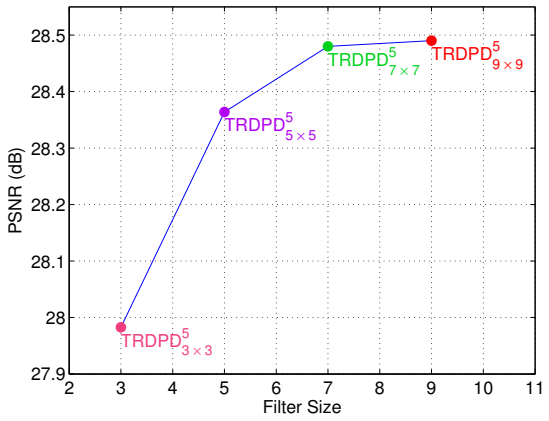

Fig. 3. Influence of the filter size.

C. Influence of Diffusion Stages

In this study, any number of diffusion stages can be exploited in our model. But in practice, the trade-off between run time and accuracy should be considered. Therefore, we need to study the influence of the number of diffusion stages on the denoising performance. $\mathrm{TRDPD}^T_{5\times5}$ and 400 images are used for training.

As shown in Fig. 4, the performance improvement becomes insignificant (≤ 0.05) when the diffusion stages ≥ 8. In order to save the training time, we choose $\mathrm{Diffusion\ Stage} = 8$ in the following experiments as it provides the best trade-off between performance and computation time.

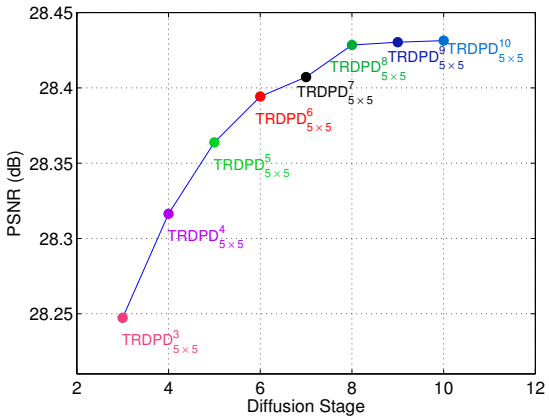

Fig. 4. Influence of the number of diffusion stages.

D. Experimental Results

By analyzing the above three subsections, we decide to employ $\mathrm{TRDPD}^8_{7\times7}$ model and 400 images for training. Meanwhile, we also test the $\mathrm{TRDPD}^8_{5\times5}$ model for comparison. Note that, the diffusion model needs to be trained respectively for different noise levels.

Examining the recovery images in Fig. 5 and Fig. 6, we see that in comparison with the other methods, the proposed algorithm is more accurate at capturing details, especially the recovery results within the red rectangle.

As shown in Fig. 5(e)-Fig. 6(e) the nonlocal technique BM3D is affected by the structured signal-like artifacts that appear in homogeneous areas of the image. This phenomenon is originated from the selection process of similar image patches in the BM3D denoising scheme. The selection process is easily influenced by the noise itself, especially in flat areas of the image, which can be dangerously self-referential. Therefore, the BM3D-based method without binning brings in the typical structured artifacts since most parts of images Image1 and Image2 are homogeneous, as shown in Fig. 5(e) and Fig. 6(e). However, the binning technique yields noisy images with lower noise level, thereby the denoised results in this case is less disturbed by the structured signal-like artifacts. Meanwhile, we find that our method introduces block-type artifacts if the peak values are relatively low, e.g., $\mathrm{peak} = 1$ in Fig. 5(g). The main reason is that our method is a local model, which becomes less effective to infer the underlying structure solely from the local neighborhoods, if the input image is too noisy.

It is also worthy noting that the SSIM values obtained by NLSPCA and BM3D using the binning technique in Fig. 5 and Fig. 6 are slight better than TRDPD. The binning operation results in a smaller Poisson image with lower resolution but higher counts per pixel. Thereby, in the extreme noise level case, the binning technique yields a significant performance increase for some images. However, the adoption of the binning technique leads to resolution reduction which will weaken or even eliminate many image details. Therefore, for the images whose most parts are homogeneous (e.g., Image1 and Image2), the recover quality will be enhanced using the binning operation because images of this kind have few easily-missed details. Overall speaking, the performance of TRDPD in terms of PSNR/SSIM is better than the other methods for peak=1, as shown in Table I. This indicates that for most images our method is more powerful in the recover quality and geometry feature preservation.

In Fig. 7-Fig. 9 are reported the recovered results for peak=2, 4 and 8 respectively. It can be observed that TRDPD and BM3D perform best on detail preservation, and achieve evidently better results in term of PSNR/SSIM index, with TRDPD even better. In the visual quality, the typical structured artifacts encountered with the BM3D-based algorithm do not appear when the proposed method TRDPD is used. Moreover, our method is more powerful in geometry-preserving, which can noticeably be visually perceived by comparison in Fig. 7-Fig. 10.

We also presented the denoising results for relatively higher peak values, e.g., peak=20 and 40 in Fig. 11 and Fig. 12 respectively. By closely visual comparison, we can observe that TRDPD recovers clearer texture and sharper edges. The similar phenomenon can also be observed within the red rectangle shown in Fig. 12(a), where TRDPD catches some tiny white features but BM3D-based method neglects them. Although these features are not quite obvious, the trained diffusion model still extracts them and exhibit these features apparently. In the TRDPD model, both the linear filters and influence functions are trained and optimized, whereby our model achieves some improvements over previous works.

Method	Peak=1	Peak=2	Peak=4	Peak=8	Peak=20	Peak=40
NLSPCA	20.90/0.491	21.60/0.517	22.09/0.535	22.38/0.545	22.54/0.549	22.56/0.550
NLSPCAbin	19.89/0.466	19.95/0.467	19.95/0.467	19.91/0.466	19.72/0.463	19.37/0.459
BM3D	21.01/0.504	22.21/0.544	23.54/0.604	24.84/0.665	26.67/0.745	28.20/0.801
BM3Dbin	21.39/0.515	22.14/0.542	22.87/0.571	23.53/0.602	24.25/0.642	24.67/0.667
$\mathrm{TRDPD}^8_{5\times5}$	21.49/0.512	22.54/0.557	23.70/0.610	24.96/0.670	26.88/0.754	28.42/0.809
$\mathrm{TRDPD}^8_{7\times7}$	**21.60/0.518**	**22.62/0.560**	**23.84/0.618**	**25.14/0.680**	**26.98/0.759**	**28.50/0.812**

TABLE I
COMPARISON OF THE PERFORMANCE OF THE TEST ALGORITHMS IN TERMS OF PSNR AND SSIM. BEST RESULTS ARE MARKED.

	BM3D	NLSPCA	$\mathrm{TRDPD}^8_{5\times5}$	$\mathrm{TRDPD}^8_{7\times7}$
256×256	1.38	367.9	1.03 (**0.01**)	2.43 (**0.02**)
512×512	4.6	1122.1	3.07 (**0.03**)	7.45 (**0.07**)

TABLE II
TYPICAL RUN TIME (IN SECOND) OF THE POISSON DENOISING METHODS FOR IMAGES WITH TWO DIFFERENT DIMENSIONS. THE CPU COMPUTATION TIME IS EVALUATED ON INTEL CPU X5675, 3.07GHZ. THE HIGHLIGHTED NUMBER IS THE RUN TIME OF GPU IMPLEMENTATION BASED ON NVIDIA GEFORCE GTX 780TI.

This critical factor of the optimized diffusion model is quite different from the FoE prior based variational model and traditional convolutional networks, where only linear filters are trained with fixed influence functions.

The recovery error in terms of PSNR (in dB) and SSIM are summarized in Table I. Comparing the indexes in Table I and the denoising results in the present figures, the best overall performance is provided by the proposed method TRDPD. We also observe that $\mathrm{TRDPD}^8_{7\times7}$ can always gain an improvement of about (0.08∼0.18dB)/(0.003∼0.01) over $\mathrm{TRDPD}^8_{5\times5}$ in terms of PSNR/SSIM. From Table I, one can see that the $\mathrm{TRDPD}^8_{7\times7}$ model outperforms the state-of-the-art BM3D-based method by (0.21∼0.41dB)/(0.003∼0.016).

E. Run Time

It is worthwhile to note that our model merely contains convolution of linear filters with an image, which offers high levels of parallelism making it well suited for GPU implementation.

In Table II, we report the typical run time of our model for the images of two different dimensions for the case of peak $= 4$. We also present the run time of two competing algorithms for a comparison [2].

Due to the structural simplicity of our model, it is well-suited to GPU parallel computation. We are able to implement our algorithm on GPU with ease. It turns out that the GPU implementation based on NVIDIA Geforce GTX 780Ti can accelerate the inference procedure significantly, as shown in Table II. By comparison, we see that our TRDPD model is generally faster than the other methods, especially with GPU implementation.

V. CONCLUSION

In our study we exploited the newly-developed trainable nonlinear reaction diffusion model in the context of Poisson noise reduction. Its critical point lies in the both training of filters and the influence functions in the reaction diffusion model by taking into account the Poisson noise statistics. Based on standard test dataset, the proposed nonlinear diffusion model provides strongly competitive results against state-of-the-art approaches, thanks to its several desired properties: anisotropy, higher order and adaptive forward/backward diffusion through the learned nonlinear functions. Moreover, the proposed model bears the properties of simple structure and high efficiency, therefore is well suited to GPU computing.

In our current work, the trained diffusion process is targeted for natural images. However, the Poisson noise often arises in applications such as astronomy imaging, biomedical imaging and fluorescence microscopy. Therefore, training specialized diffusion process for specific images bears the potential to improve the current results. This could be our future study.

[2] All the methods are run in Matlab with single-threaded computation for CPU implementation. We only consider the version without binning technique.

REFERENCES

[1] F. J. Anscombe. The transformation of Poisson, binomial and negative-binomial data. *Biometrika*, pages 246–254, 1948.

[2] R. Berry and J. Burnell. Astronomical image processing. *Willman-Bell, Inc*, 2000.

[3] M. Bertero, P. Boccacci, G. Talenti, R. Zanella, and L. Zanni. A discrepancy principle for Poisson data. *Inverse Problems*, 26(10):105004, 2010.

[4] Y. Chen, W. Yu, and T. Pock. On learning optimized reaction diffusion processes for effective image restoration. In *Proc. IEEE Conference on Computer Vision and Pattern Recognition (CVPR)*, 2015.

[5] I. Csiszár. Why least squares and maximum entropy? an axiomatic approach to inference for linear inverse problems. *The Annals of Statistics*, 19(4):2032–2066, 1991.

[6] K. Dabov, A. Foi, V. Katkovnik, and K. O. Egiazarian. Image denoising by sparse 3-d transform-domain collaborative filtering. *IEEE Trans. Image Process.*, 16(8):2080–2095, 2007.

[7] A. Danielyan, V. Katkovnik, and K. Egiazarian. Deblurring of Poissonian images using BM3D frames. In *SPIE Optical Engineering+ Applications*, pages 813812–813812. International Society for Optics and Photonics, 2011.

[8] D. L. Donoho. Nonlinear wavelet methods for recovery of signals, densities, and spectra from indirect and noisy data. In *Proceedings of symposia in Applied Mathematics*, volume 47, pages 173–205. Providence: American Mathematical Society, 1993.

[9] M. A. Figueiredo and J. M. Bioucas-Dias. Restoration of Poissonian images using alternating direction optimization. *IEEE Trans. Image Process.*, 19(12):3133–3145, 2010.

[10] M. Fisz. The limiting distribution of a function of two independent random variables and its statistical application. In *Colloquium Mathematicae*, volume 3, pages 138–146. Institute of Mathematics Polish Academy of Sciences, 1955.

[11] E. Gil-Rodrigo, J. Portilla, D. Miraut, and R. Suarez-Mesa. Efficient joint Poisson-Gauss restoration using multi-frame ℓ_2-relaxed-ℓ_0 analysis-based sparsity. In *Image Processing (ICIP), 2011 18th IEEE International Conference on*, pages 1385–1388. IEEE, 2011.

[12] R. Giryes and M. Elad. Sparsity-based Poisson denoising with dictionary learning. *IEEE Trans. on Image Processing*, 23(12):5057–5069, 2014.

[13] A. Graves and J. Schmidhuber. Offline handwriting recognition with multidimensional recurrent neural networks. In *Proc. 15th NIPS*, pages 545–552, 2009.

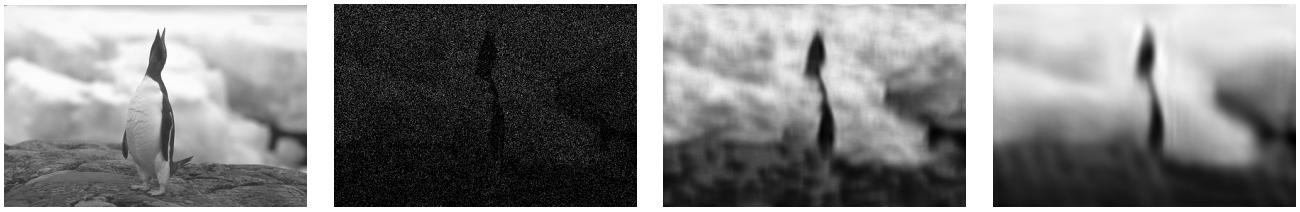

(a) Image 1 (b) Noisy image. Peak=1 (c) NLSPCA (24.09/0.682) (d) NLSPCAbin (22.77/0.719)

(e) BM3D (22.92/0.636) (f) BM3Dbin (24.57/**0.730**) (g) $\mathrm{TRDPD}^{8}_{5\times5}$ (24.65/0.701) (h) $\mathrm{TRDPD}^{8}_{7\times7}$ (**24.94**/0.725)

Fig. 5. Denoising of Image 1 with peak=1. The results are reported by PSNR/SSIM index. Best results are marked.

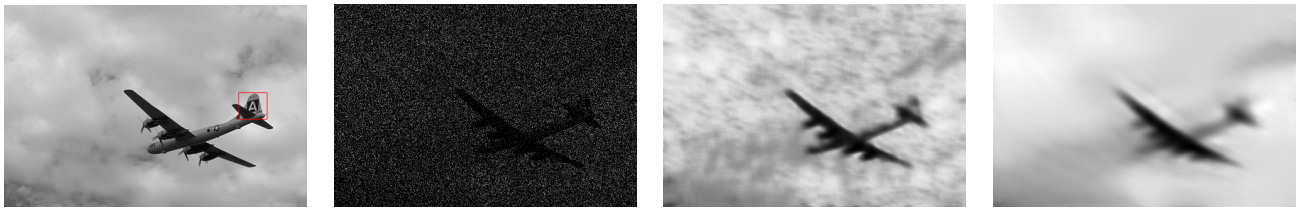

(a) Image 2 (b) Noisy image. Peak=1 (c) NLSPCA (24.76/0.858) (d) NLSPCAbin (23.25/0.908)

(e) BM3D (24.23/0.881) (f) BM3Dbin (25.66/**0.913**) (g) $\mathrm{TRDPD}^{8}_{5\times5}$ (25.53/0.876) (h) $\mathrm{TRDPD}^{8}_{7\times7}$ (**26.13**/0.900)

Fig. 6. Denoising of Image 2 with peak=1. The results are reported by PSNR/SSIM index. Best results are marked.

[14] Z. T. Harmany, R. F. Marcia, and R. M. Willett. This is SPIRAL-TAP: sparse Poisson intensity reconstruction algorithmstheory and practice. *IEEE Trans. Image Process.*, 21(3):1084–1096, 2012.

[15] K. He, X. Zhang, S. Ren, and J. Sun. Delving deep into rectifiers:surpassing human-level performance on imagenet classification. In *Int'l Conf. Computer Vision*, 2015.

[16] V. Jain and S. Seung. Natural image denoising with convolutional networks. In *NIPS*, pages 769–776, 2009.

[17] T. Le, R. Chartrand, and T. J. Asaki. A variational approach to reconstructing images corrupted by Poisson noise. *Journal of Mathematical Imaging and Vision*, 27(3):257–263, 2007.

[18] Y. LeCun, L. Bottou, Y. Bengio, and P. Haffner. Gradient-based learning applied to document recognition. *Proceedings of the IEEE*, 86(11):2278–2324, 1998.

[19] S. Lefkimmiatis, P. Maragos, and G. Papandreou. Bayesian inference on multi-scale models for Poisson intensity estimation: Applications to photon-limited image denoising. *IEEE Trans. Image Process.*, 18(8):1724–1741, 2009.

[20] D. J. Lingenfelter, J. A. Fessler, and Z. He. Sparsity regularization for image reconstruction with Poisson data. In *IS&T/SPIE Electronic Imaging*, pages 72460F–72460F. International Society for Optics and Photonics, 2009.

[21] D. C. Liu and J. Nocedal. On the limited memory BFGS method for large scale optimization. *Mathematical Programming*, 45(1):503–528, 1989.

[22] F. Luisier, C. Vonesch, T. Blu, and M. Unser. Fast interscale Wavelet denoising of Poisson-corrupted images. *Signal Processing*, 90(2):415–427, 2010.

[23] M. Makitalo and A. Foi. Optimal inversion of the Anscombe transformation in low-count Poisson image denoising. *IEEE Trans. Image Process.*, 20(1):99–109, 2011.

[24] D. Martin, C. Fowlkes, D. Tal, and J. Malik. A database of human segmented natural images and its application to evaluating segmentation algorithms and measuring ecological statistics. In *Proc. 8th Int'l Conf. Computer Vision*, volume 2, pages 416–423, July 2001.

[25] C. Michael, D. Sanjoy, and R. E. Schapire. A generalization of principal components analysis to the exponential family. In *NIPS*, pages 617–624, 2002.

[26] Y. Nesterov. *Introductory lectures on convex optimization*, volume 87 of *Applied Optimization*. Kluwer Academic Publishers, Boston, MA, 2004. A basic course.

[27] I. Rodrigues, J. Sanches, and J. Bioucas-Dias. Denoising of medical images corrupted by Poisson noise. In *Image Processing, 15th IEEE International Conference on*, pages 1756–1759. IEEE, 2008.

[28] S. Roth and M. J. Black. Fields of experts. *IJCV*, 82(2):205–229, 2009.

[29] J. Salmon, Z. Harmany, C.-A. Deledalle, and R. Willett. Poisson noise reduction with non-local PCA. *Journal of Mathematical Imaging and Vision*, 48(2):279–294, 2014.

[30] Z. Wang, A. C. Bovik, H. R. Sheikh, and E. P. Simoncelli. Image quality assessment: from error visibility to structural similarity. *IEEE Trans. Image Process.*, 13(4):600–612, 2004.

[31] R. M. Willett and R. D. Nowak. Multiscale Poisson intensity and density

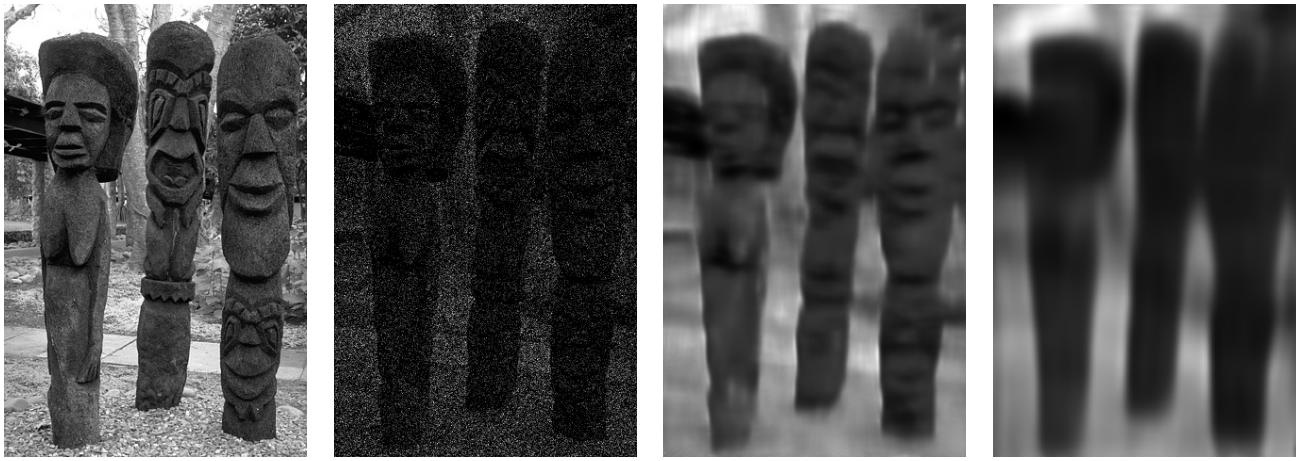

(a) Image 3 (b) Noisy image. Peak=2 (c) NLSPCA (19.63/0.307) (d) NLSPCAbin (18.14/0.240)

(e) BM3D (20.16/0.371) (f) BM3Dbin (19.95/0.340) (g) $\mathrm{TRDPD}^{8}_{5\times5}$ (20.49/0.389) (h) $\mathrm{TRDPD}^{8}_{7\times7}$ (**20.52/0.393**)

Fig. 7. Denoising of Image 3 with peak=2. The results are reported by PSNR/SSIM index. Best results are marked.

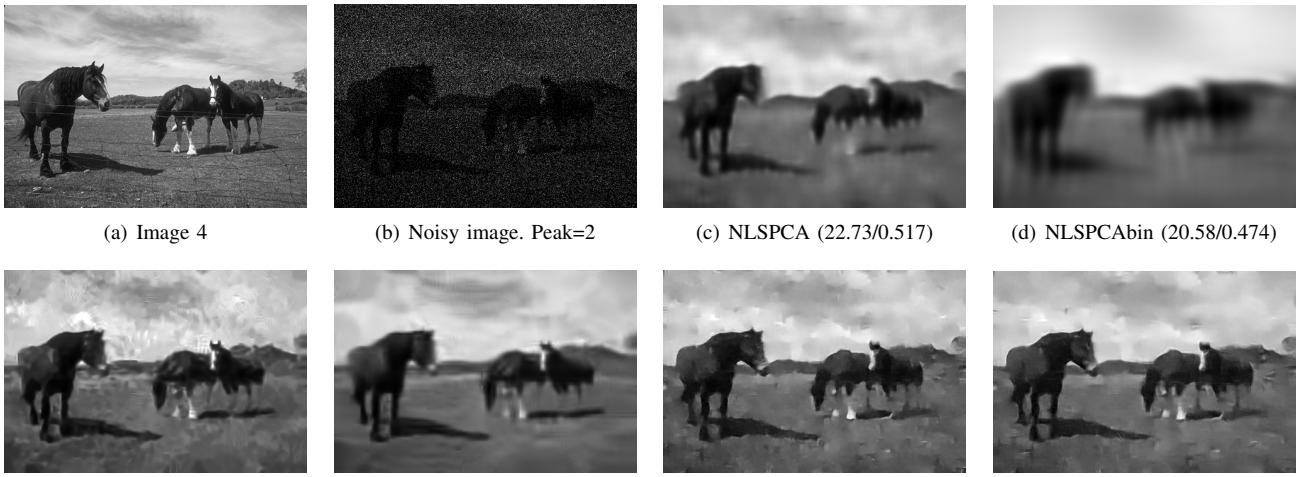

(a) Image 4 (b) Noisy image. Peak=2 (c) NLSPCA (22.73/0.517) (d) NLSPCAbin (20.58/0.474)

(e) BM3D (23.10/0.502) (f) BM3Dbin (23.24/0.537) (g) $\mathrm{TRDPD}^{8}_{5\times5}$ (23.64/0.554) (h) $\mathrm{TRDPD}^{8}_{7\times7}$ (**23.74/0.558**)

Fig. 8. Denoising of Image 4 with peak=2. The results are reported by PSNR/SSIM index. Best results are marked.

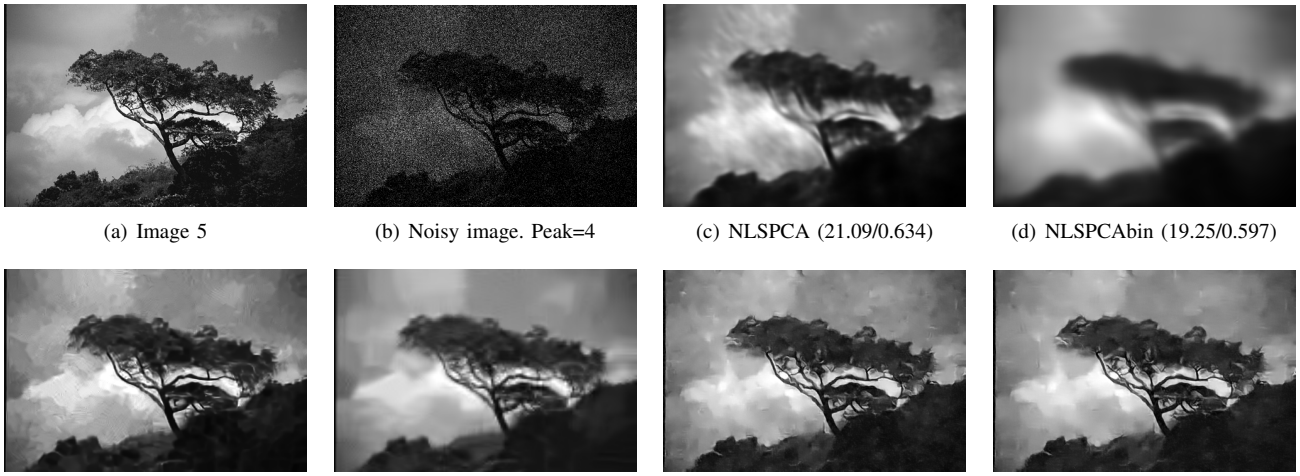

(a) Image 5 (b) Noisy image. Peak=4 (c) NLSPCA (21.09/0.634) (d) NLSPCAbin (19.25/0.597)

(e) BM3D (23.29/0.655) (f) BM3Dbin (22.22/0.666) (g) $\mathrm{TRDPD}^{8}_{5\times5}$ (23.73/0.702) (h) $\mathrm{TRDPD}^{8}_{7\times7}$ (**23.83/0.714**)

Fig. 9. Denoising of Image 5 with peak=4. The results are reported by PSNR/SSIM index. Best results are marked.

(a) Image 6 (b) Noisy image. Peak=8 (c) NLSPCA (20.49/0.756) (d) NLSPCAbin (17.60/0.328)

(e) BM3D (23.20/0.596) (f) BM3Dbin (21.62/0.499) (g) $\mathrm{TRDPD}^{8}_{5\times5}$ (23.61/0.610) (h) $\mathrm{TRDPD}^{8}_{7\times7}$ (**23.68/0.617**)

Fig. 10. Denoising of Image 6 with peak=8. The results are reported by PSNR/SSIM index. Best results are marked.

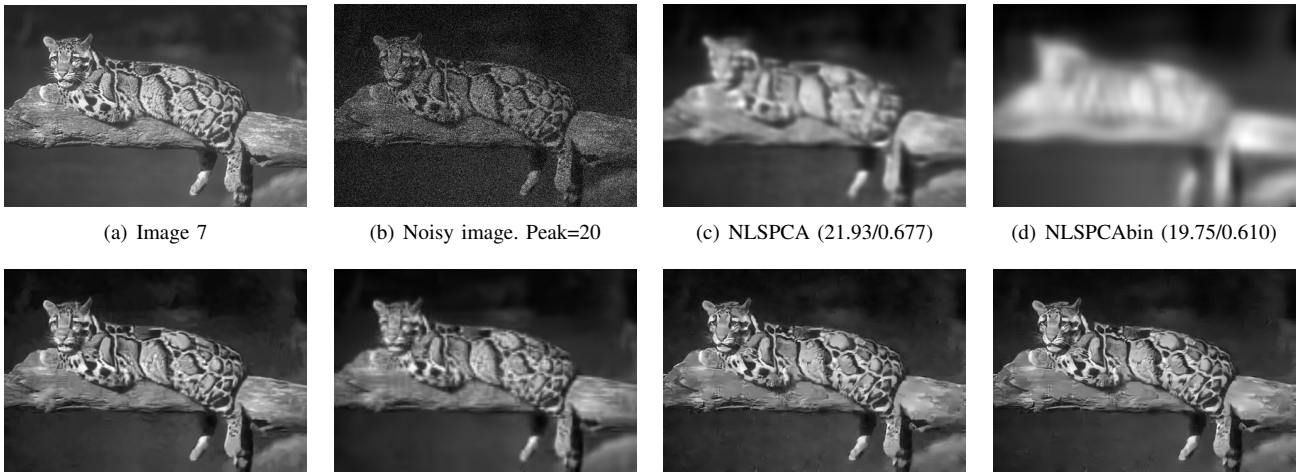

(a) Image 7 (b) Noisy image. Peak=20 (c) NLSPCA (21.93/0.677) (d) NLSPCAbin (19.75/0.610)

(e) BM3D (26.76/0.847) (f) BM3Dbin (24.33/0.775) (g) $\mathrm{TRDPD}^{8}_{5\times5}$ (26.88/0.846) (h) $\mathrm{TRDPD}^{8}_{7\times7}$ (**27.01/0.856**)

Fig. 11. Denoising of Image 7 with peak=20. The results are reported by PSNR/SSIM index. Best results are marked.

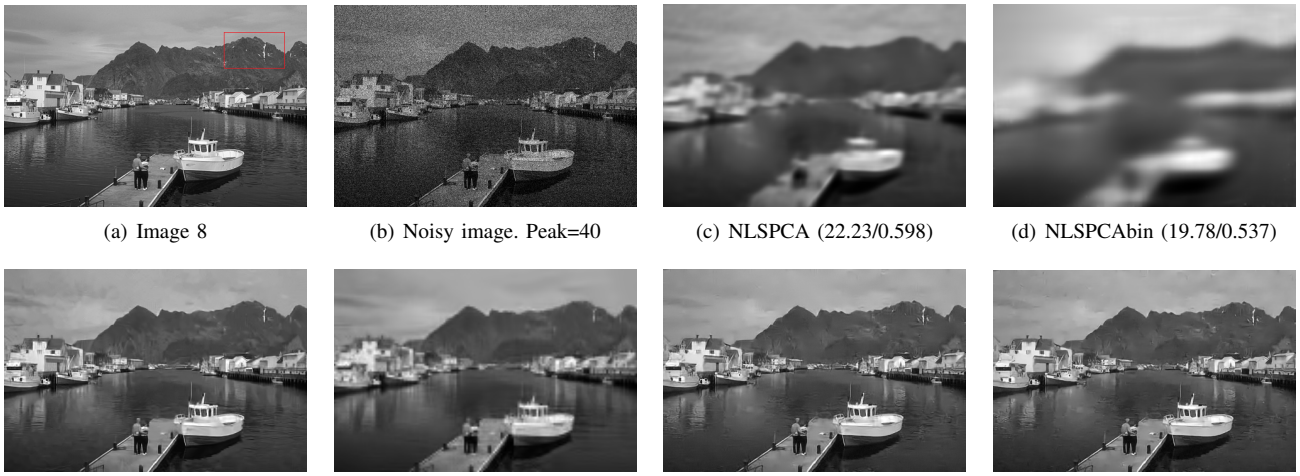

(a) Image 8 (b) Noisy image. Peak=40 (c) NLSPCA (22.23/0.598) (d) NLSPCAbin (19.78/0.537)

(e) BM3D (28.67/0.799) (f) BM3Dbin (24.25/0.678) (g) $\mathrm{TRDPD}^{8}_{5\times5}$ (28.94/**0.807**) (h) $\mathrm{TRDPD}^{8}_{7\times7}$ (**29.06/0.809**)

Fig. 12. Denoising of Image 8 with peak=40. The results are reported by PSNR/SSIM index. Best results are marked.

estimation. *IEEE Trans. Inf. Theory*, pages 3171–3187, 2007.

[32] B. Zhang, J. M. Fadili, and J.-L. Starck. Wavelets, ridgelets, and curvelets for Poisson noise removal. *IEEE Trans. Image Process.*, 17(7):1093–1108, 2008.

[33] X. Zhang, Y. Lu, and T. Chan. A novel sparsity reconstruction method from Poisson data for 3d bioluminescence tomography. *Journal of Scientific Computing*, 50(3):519–535, 2012.